Electron-ion thermal equilibration after spherical shock collapse

J. R. Rygg,* J. A. Frenje, C. K. Li, F. H. Séguin, and R. D. Petrasso†
Plasma Science and Fusion Center, Massachusetts Institute of Technology, Cambridge, Massachusetts 02139, USA

D. D. Meyerhofer‡ and C. Stoeckl
Laboratory for Laser Energetics, University of Rochester, Rochester, New York 14623, USA

(Received 3 March 2009; published 25 August 2009)

A comprehensive set of dual nuclear product observations provides a snapshot of imploding inertial confinement fusion capsules at the time of shock collapse, shortly before the final stages of compression. The collapse of strong convergent shocks at the center of spherical capsules filled with D_2 and ^{3}He gases induces D-D and D-^{3}He nuclear production. Temporal and spectral diagnostics of products from both reactions are used to measure shock timing, temperature, and capsule areal density. The density and temperature inferred from these measurements are used to estimate the electron-ion thermal coupling and demonstrate a lower electron-ion relaxation rate for capsules with lower initial gas density.

DOI: 10.1103/PhysRevE.80.026403 PACS number(s): 52.35.Tc, 52.25.Fi, 52.70.Nc, 52.57.−z

I. INTRODUCTION

Converging spherical shocks and electron-ion thermal equilibration are basic physical processes [1] of fundamental importance for the design of high gain implosions in inertial confinement fusion (ICF) [2–4]. Strong, spherically convergent shocks are formed by the rapid deposition of energy in the form of lasers (direct drive) or x rays (indirect drive) on the surface of a spherical capsule. Current "hot-spot" ICF ignition designs include a sequence of up to four convergent shocks that must be precisely timed to coalesce at the inner-shell surface so as to obtain maximal shell compression [5,6], a necessity for high fusion gain. Other ignition designs include the launching of a convergent shock into a compressed fuel assembly [7]. In both cases, ICF implosion design and performance is deeply affected by the speed and heating of convergent shocks through ambient and compressed materials.

Shocks initially deposit thermal energy primarily in the ions and the ensuing electron-ion thermal equilibration is one of many related transport processes of concern for ICF modelers [3,4]. Recent theoretical [8–10] and computational [11–13] works have helped to clarify ambiguities in the Landau-Spitzer energy equilibration rate [14,15], which result from *ad hoc* cutoffs of logarithmic divergences in the Coulomb collisional rates. Previous experimental and observational investigations of electron-ion thermal relaxation include the works of Celliers *et al.* [16,17] and Laming *et al.* [18] and new investigations are currently underway [19,20].

This paper presents the first results of temporal and spectral measurements of products from two simultaneous nuclear reaction types induced by the central collapse of convergent shocks. Nuclear measurements of some aspects of shock collapse using a single nuclear product have been reported recently [21–23]. Observations of these products supply compelling information about the speed and heating of the shocks and the state of the imploding capsule at the time of shock collapse. In the experiments discussed here, this occurs immediately before the onset of the deceleration phase and the final stages of compression. The comprehensive picture of the central shocked gas provided by the dual nuclear reaction measurements is used to evaluate electron-ion thermal equilibration in the plasma after shock collapse.

Section II describes the experimental setup and Sec. III the experimental results. Various plasma parameters of the central shocked gas are derived from the measurements in Sec. IV. A brief review of electron-ion thermal equilibration after shock heating is outlined in Sec. V and is applied to the experimental observations in Sec. VI. Concluding remarks are presented in Sec. VII.

II. EXPERIMENTAL SETUP

Direct-drive spherical capsule implosions were conducted using the OMEGA laser system [24], with 60 beams of ultraviolet (351 nm) light in a 1 ns square pulse, a total energy of 23 kJ, and full single-beam smoothing [25]. The resulting 1×10^{15} W/cm^2 intensity was incident on capsules with diameters between 855 and 875 μm, plastic (density 1.04 g/cm^3) shell thicknesses (ΔR) of 20, 24, or 27 μm, and a flash coating of 0.1 μm of aluminum. The capsules were filled with an equimolar (by atom) mixture of D_2 and ^{3}He gasses with a total fill pressure of 3.6 or 18 atm at 293 K, corresponding to initial gas mass densities (ρ_0) of 0.5 and 2.5 mg/cm^3, respectively.

Three distinct primary nuclear reactions occur during capsule implosions with D_2 and ^{3}He fuel

$$D + D \rightarrow {}^3He + n, \tag{1}$$

$$D + D \rightarrow T + p, \tag{2}$$

*Present address: Lawrence Livermore National Laboratory, 7000 East Avenue, Livermore, California 94550, USA.
†Also at Laboratory for Laser Energetics, University of Rochester, Rochester, New York 14623, USA.
‡Also at Department of Mechanical Engineering, University of Rochester, Rochester, New York 14623, USA; and Department of Physics and Astronomy, University of Rochester, Rochester, New York 14623, USA.

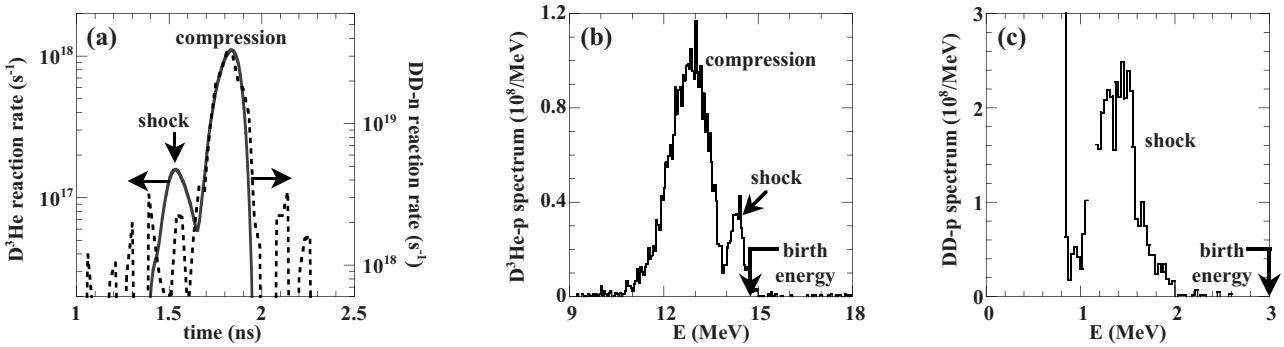

FIG. 1. Representative experimental observations of DD and D ^{3}He nuclear products emitted at shock- and compression-bang times from an implosion of a 24-μm-thick CH capsule shell filled with 2.5 mg/cm^3 of D_2-^{3}He gas (OMEGA shot 38525). (a) D^{3}He (solid) and DD-*n* (dotted) reaction-rate histories. (b) D ^{3}He proton spectrum. (c) DD-proton spectrum.

$$D + {}^3He \rightarrow {}^4He + p. \quad (3)$$

The neutron (1) and proton (2) branches of the DD reaction have nearly equal probabilities over temperatures of interest. The D ^{3}He reaction depends much more strongly on temperature due to the doubly-charged ^{3}He reactant [26]. The mean birth energies of D ^{3}He and DD protons are 14.7 and 3.0 MeV, respectively.

Nuclear products were observed using the proton and neutron temporal diagnostics (PTD and NTD) [22,27] to measure the D ^{3}He and DD-*n* reaction histories, multiple wedge-range-filter proton spectrometers [28] to measure the D ^{3}He proton yield and spectrum, and a magnet-based charged-particle spectrometer [28] to obtain the first measurements of DD protons emitted at shock-bang time.

The D ^{3}He reaction-rate history shows two distinct times of nuclear production [Fig. 1(a)]: "shock-burn" begins shortly after shock collapse and ends near the beginning of the deceleration of the shell and "compression-burn" lags about 300 ps after shock burn, beginning near the onset of shell deceleration and lasting approximately until the stagnation of the imploding shell (Fig. 2). For ordinary D_2-^{3}He mixtures, the DD-*n* reaction rate during the shock burn is below the diagnostic detection threshold.

The shock and compression components can often be distinguished in D ^{3}He proton spectra [Fig. 1(b)] [21]. The protons emitted during shock-burn experience relatively little downshift (~0.4 MeV) due to the low total capsule areal density (ρR) at that time. The shell continues to compress after shock-burn ends and by the time of compression-burn, the ρR has increased enough to downshift D ^{3}He protons by several MeV.

The ρR during shock-burn is low enough to allow nascent 3.0 MeV DD protons to escape the capsule [Fig. 1(c)], but the DD protons are ranged out in the capsule during compression-burn due to the higher capsule ρR at that time. Measurement of DD protons emitted during shock-burn provides a valuable and sole measurement of the DD shock yield when the reaction rate is below the NTD threshold (as is often the case). Measurement of their downshift provides a double check on the ρR at shock-bang time inferred using the D ^{3}He proton spectra or the sole measurement in cases where the shock component of the D^{3}He proton spectrum cannot be separated from the compression component.

III. EXPERIMENTAL RESULTS

Measured shock-bang times and D ^{3}He and DD-*p* shock yields are shown in Fig. 3 as a function of ΔR for implosions of capsules with different ρ_0 (see also Table I). The shock-bang time (t_s) is the time of peak D ^{3}He nuclear production during the shock-burn phase, the shock-burn duration (Δt_s) is the full temporal width at half the maximum shock-burn production rate, the D ^{3}He shock yield ($Y_{D\,^3He}$) includes only the contribution from the higher-energy "shock" component of the D ^{3}He-proton spectrum, and the DD-*p* shock yield (Y_{DD}) includes only that part of the spectrum above the high-energy cutoff of protons accelerated from the shell [29] [seen at 0.8 MeV in Fig. 1(c)]. Figure 3 plots the mean and the standard deviation of the mean for implosion ensembles of each capsule configuration. Shot-by-shot tables of most of the experimental results are available in Ref. [30].

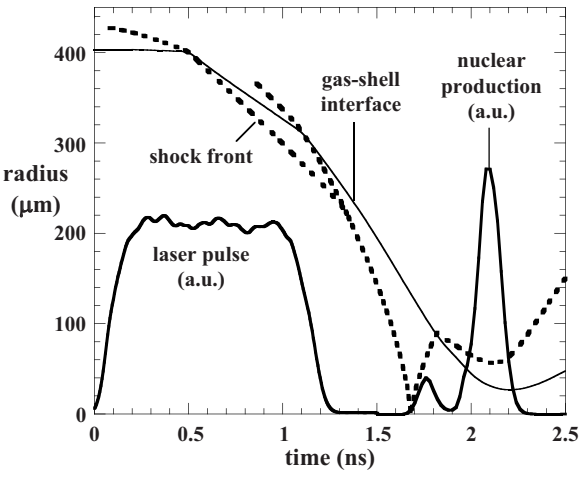

FIG. 2. A representative 1D simulation shows the D ^{3}He nuclear reaction rate and trajectories of the gas-shell interface and the converging shock. Collapse of the converging shock induces nuclear shock-burn about 300 ps before the compression-burn peak and stagnation of the imploding shell. Reprinted with permission from Ref. [23]. Copyright 2008, American Institute of Physics.

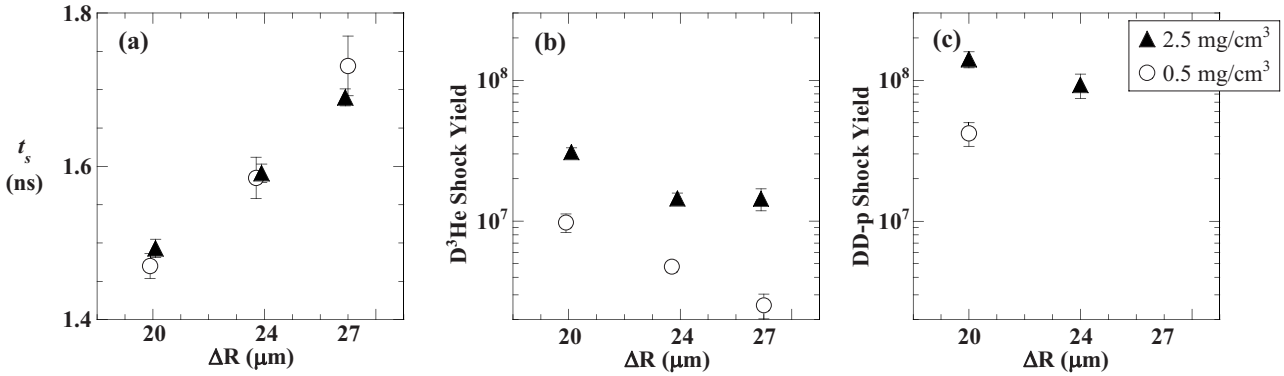

FIG. 3. Experimental observations of (a) shock-bang time, (b) D ^{3}He shock yield, and (c) DD-p shock yield as a function of capsule shell thickness for ensembles of capsules filled with 2.5 (triangles) or 0.5 mg/cm^3 (circles) of D ^{3}He gas. In some cases, the error bars (representing the standard error of the ensemble mean) are smaller than the marker size.

Experiments show that t_s is linearly delayed with increasing ΔR [Fig. 3(a)]. No difference in t_s was observed for capsules with different ρ_0. For capsules with the same ΔR, identical shocks should be generated in the shell with identical drive conditions (as is approximately the case here) and the shocks should break into the gas at the same time. Since t_s is independent of ρ_0, we conclude that shocks of the same speed are launched into the gas for implosions with the same ΔR and drive.

Both D ^{3}He and DD shock yields were observed to decrease for implosions of targets with thicker shells and lower ρ_0. However, the expected yield reduction—due only to the density dependence of the nuclear fusion rate—from high to low ρ_0 is 25, a much higher value than the observed reduction of between 3 and 5. This indicates that lower fill density also results in reduced thermal coupling between ions and electrons (see Sec. V) so that the ion temperature, and consequently the nuclear fusion rate, remains high.

The average ion temperature [31] at shock-bang time T_{si} can be inferred using the measured yields of the two different nuclear reactions based on the ratio of their respective thermal reactivities [26]. This method has previously been used to infer ion temperature during the compression burn by Li *et al.* [32] and Frenje *et al.* [22]. Figure 4 plots the T_{si} inferred by this method, showing higher T_{si} for low ρ_0 implosions.

The compression of the capsule at shock-bang time can be quantified by the shock-burn-averaged [31] areal density, ρR_s. The areal density at shock time is of particular concern in ICF because the value of ρR_s sets the initial condition for the final capsule compression to the stagnation ρR, which in turn is a fundamental metric of capsule assembly and is essential for ignition and efficient nuclear burn [2–4]. Experimentally, ρR_s is inferred from the measured mean energy downshift from the birth energy of DD protons ($\rho R_{s,\mathrm{DD}}$) or D ^{3}He protons in the shock line ($\rho R_{s,\mathrm{D}\,^3\mathrm{He}}$), using a theoretical formalism to relate their energy loss to plasma parameters [28,33]. The inferred ρR_s value is insensitive to the exact parameter values assumed, particularly when using the downshift of 14.7 MeV D ^{3}He protons; a CH plasma density of 3 g/cm^3 and temperature of 0.3 keV were used to derive the quoted ρR_s values.

Substantial agreement is observed between ρR_s inferred from spectral results obtained using both DD and D ^{3}He protons, as seen in Fig. 5 and Table I. Implosions with increasing ΔR show an increase in ρR_s due to the larger remaining shell mass at shock time. On the basis of physical principles, the contribution of the shell to the areal density $\rho R_{s,\mathrm{shell}}$ should be only weakly dependent on the initial gas density ρ_0 since the trajectory of the high-density shell will be almost unaffected by the fill gas until the shell starts to decelerate

TABLE I. Mean and standard deviation of the mean of shock measurements with D ^{3}He and DD protons for implosion ensembles of different initial gas density (ρ_0) and capsule shell thickness (ΔR). Each ensemble consists of N (N_{DD}) implosions with D ^{3}He (DD-p) measurements. The D ^{3}He ensemble includes shock-bang time (t_s), shock-burn duration (Δt_s), D ^{3}He shock yield ($Y_{\mathrm{D}\,^3\mathrm{He}}$), shock areal-density ($\rho R_{s\text{-}d\,^3\mathrm{He}}$), and inferred gas compression ratio (ρ_s/ρ_0[D ^{3}He]). The remaining quantities are from the DD ensemble, including the DD-p shock yield (Y_{DD}), and the shock-burn-averaged ion temperature (T_{si}).

ρ_0 (mg/cc)	ΔR (μm)	Diam. (μm)	N (N_{DD})	t_s (ps)	Δt_s (ps)	$Y_{\mathrm{D}\,^3\mathrm{He}}$ ($\times 10^7$)	Y_{DD} ($\times 10^7$)	T_{si} (keV)	$\rho R_{s\text{-}d\,^3\mathrm{He}}$ (mg/cm^2)	$\rho R_{s\text{-}dd}$ (mg/cm^2)	ρ_s/ρ_0 [D^{3}He]	ρ_s/ρ_0 [DD]
0.5	19.9	862	8(5)	1470 ± 16	129 ± 18	0.98 ± 15%	4.2 ± 10%	7.7 ± 0.7		8.3 ± 0.7		22 ± 3
0.5	23.7	873	6(0)	1585 ± 27	129 ± 11	0.48 ± 9%			9.8 ± 0.4		17 ± 1	
0.5	27.0	873	4(0)	1731 ± 39	122 ± 30	0.25 ± 20%			12.0 ± 0.9		17 ± 2	
2.5	20.1	863	8(3)	1493 ± 12	145 ± 13	3.09 ± 7%	14.1 ± 13%	5.8 ± 0.3	8.2 ± 1.0	9.3 ± 0.6	18 ± 3	23 ± 3
2.5	23.9	865	9(3)	1591 ± 12	137 ± 10	1.45 ± 9%	9.2 ± 20%	5.4 ± 0.4	9.1 ± 0.7	10.0 ± 0.7	14 ± 1	16 ± 2
2.5	26.9	873	6(2)	1690 ± 11	146 ± 10	1.44 ± 18%			9.4 ± 1.2	11.1 ± 1.0	14 ± 2	15 ± 2

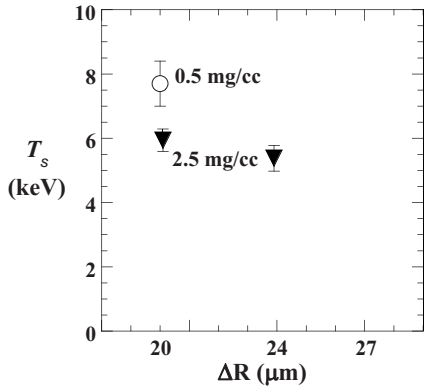

FIG. 4. Shock-burn-averaged ion temperature vs ΔR for two different ρ_0, calculated using the ratio of measured DD-p to D^{3}He shock yields. Although shocked to the same initial ion temperature at a given shell thickness, thermal coupling with electrons is weaker in the low ρ_0 implosions.

several hundred picoseconds after shock-bang time. As we will see in Sec. IV, ρR_s is dominated by the shell contribution and should also be weakly dependent on ρ_0. The data shown in Fig. 5 and Table I are consistent with this viewpoint.

IV. CHARACTERIZATION OF THE SHOCKED GAS

Theoretical analysis suggests that converging shocks are weakly unstable to initial asymmetries [34]; however, experiments have demonstrated that the nuclear observables are highly robust to drive asymmetries [23] and that the growth of asymmetries due to hydrodynamic instabilities is insufficient to mix the shell with the fill gas at during the shock-burn [35]. Thus, the behavior of the imploding capsule at the time of shock-burn can be well described by a one-dimensional (1D), spherically symmetric model.

The shock-burn-averaged plasma density ρ_s can be estimated from our measurements of the shock-burn-averaged total areal density ρR_s. Assuming thin shells and a spherically symmetric model of the implosion and invoking mass conservation gives

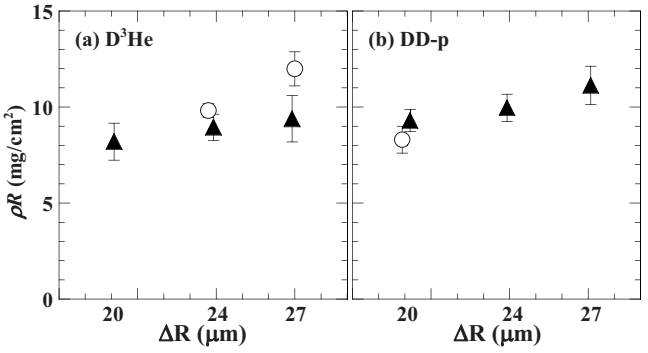

FIG. 5. Shock-burn-averaged areal density ρR_s vs ΔR for D ^{3}He fills of 2.5 mg/cm^3 (triangles) and 0.5 mg/cm^3 (circles). ρR_s is inferred from the downshift of nascent (a) 14.7 MeV D ^{3}He protons and (b) 3 MeV DD protons from their birth energy. Markers show mean and standard error.

$$\frac{\rho_s}{\rho_0} = \left(\frac{\rho R_s}{\rho R_{0,\mathrm{gas}} + f \rho R_{0,\mathrm{shell}}} \right)^{3/2}, \tag{4}$$

where $\rho R_{0,\mathrm{gas}}$ and $\rho R_{0,\mathrm{shell}}$ are the initial areal densities of the gas and the shell before the implosion and f is the fraction of the initial shell mass remaining after ablation of the outer shell by the drive laser intensity. The mass ablation rate dm/dt is [3,4]

$$\frac{dm}{dt}(\mathrm{g/cm^2/s}) = 2.6 \times 10^5 \left(\frac{I_{15}}{\lambda^4} \right)^{1/3}, \tag{5}$$

where I_{15} is the laser intensity in 10^{15} W/cm^2 and λ is the laser wavelength in microns. For these experiments, about 10 μm of the original shell is ablated during the laser pulse, giving a volumetric compression ratio at shock time ρ_s/ρ_0 of 14–23 (see Table I). The inferred compression ratios are apparently equal for implosions with the same ΔR but different ρ_0, which is consistent with the expectation stated in the previous section.

Using these values of the compression ratio, mass conservation can be used to estimate the areal density of the fuel at shock time $\rho R_{s,\mathrm{gas}}$,

$$\rho R_{s,\mathrm{gas}} = \rho R_{0,\mathrm{gas}} \left(\frac{\rho_s}{\rho_0} \right)^{2/3}, \tag{6}$$

which gives values of 0.15 and 0.6–0.8 mg/cm^2, contributing 1%–2% and 6%–9% of the total ρR_s for low and high ρ_0, respectively.

Simultaneous knowledge of the gas composition, density, and temperature allows some basic plasma parameters to be computed. For definiteness, the following discussion is restricted to the case of the $\Delta R = 20$ μm ensemble with high (low) ρ_0. The DD-inferred compression ratio, ~22, is the same for all ρ_0, but is slightly higher than the D ^{3}He inferred compression ratio, 18, for high ρ_0. The average of these methods gives a compression ratio $\rho_s/\rho_0 = 20$, which will be used for both ensembles. In this case, at shock-bang time, the mass density $\rho_s = 50(10)$ mg/cm^3, the electron density $n_e = 18(3.6) \times 10^{21}$ cm^{-3}, and the Fermi energy $E_f = \hbar^2 (3\pi^2 n_e)^{2/3}/2m_e = 2.5(0.86)$ eV, where $\hbar$ is the reduced Planck constant and m_e is the electron mass.

As will be shown in Sec. V, the electron temperature T_e averaged over shock-burn is 2.0 (0.73) keV, which establishes that the electrons can be treated as nondegenerate: the electron degeneracy parameter $\Theta = T_e/E_f = 800(850) \gg 1$. Both the electron and ion temperatures are much higher than the final ionization energies of atomic D and ^{3}He (D: 13.6 eV, ^{3}He: 54.4 eV), so the gas is a fully ionized plasma.

The pressure in a nondegenerate fully ionized plasma is given by the ideal kinetic gas pressure, $P = (n_e T_e + n_i T_i) = 17(3.4)$ TPa. As temperatures in this paper are expressed in energy units, Boltzmann's constant k_B has been suppressed. The plasma parameter, related to the number of particles in a Debye sphere, is $(\varepsilon_0 T_e / e^2 n_e^{1/3})^{3/2} = 1900(950) \gg 1$. ε_0 is the permittivity of free space and e is the fundamental charge.

The Coulomb logarithm, $\ln \Lambda = \ln(b_{\max}/b_{\min})$, is important for many plasma transport properties, including thermal equilibration, but there is some variation in the precise impact-parameter cutoffs $b_{\max}$ and $b_{\min}$ [13,15]. Here, we use the value of $\ln \Lambda$ given by Ref. [10] in the nondegenerate limit

$$\ln \Lambda = \ln\left(\frac{T_e}{\hbar \omega_{pe}}\right) - 1.8283, \tag{7}$$

where $\omega_{pe} = (e^2 n_e/\varepsilon_0 m_e)^{1/2}$ is the electron plasma frequency. For the gas at shock time, Eq. (7) gives $\ln \Lambda = 6.2(6.0)$.

It should be emphasized that this characterization of the shocked gas completely ignores many attributes of this highly dynamic and nonuniform system, including steep temperature and density gradients, nonthermal velocity components, and rapid temporal evolution. However, describing the plasma in this "shock-averaged" manner [31] offers valuable information about the state of the imploding capsule immediately before the onset of deceleration phase, both as an initial condition of and in contrast to the compression burn. In addition, comparison of the shock states with different ρ_0 allows the value of the electron-ion thermal equilibration rate to be inferred experimentally.

V. THERMAL EQUILIBRATION

If a strong, nonradiating shock propagating at speed u_s through a uniform ideal gas is sufficiently strong to fully ionize the gas (as is the case here), it will distribute thermal energy among the electron and ion species according to their masses m_j, such that the immediate post-shock temperatures T_{0j} are (e.g., see Ref. [36])

$$T_{0j} = \frac{3}{16} m_j u_s^2, \tag{8}$$

where $j = e, i$ for electrons and ions.

The large mass difference between the ions and electrons (~4600 for the equimolar D-^{3}He mixture considered here) endows each species with widely different initial temperatures, but otherwise depends only on the shock speed. The electron and ion temperatures (T_e and T_i) relax over time to a final equilibrium temperature T_f as energy is exchanged through Coulomb collisions. In the absence of thermal conduction, the sum of T_e and T_i is constrained by energy conservation according to their relative heat capacities

$$T_i + ZT_e = T_{0i} + ZT_{0e} = (1+Z)T_f, \tag{9}$$

where $Z = 1.5$ is the average ion atomic number. Note that $ZT_{0e} \ll T_{0i}$.

The rate of temperature equilibration is usually expressed as the ratio of the temperature difference over a characteristic time [1,15]

$$\frac{dT_e}{dt} = \frac{T_i - T_e}{\tau_{ei}}, \tag{10}$$

where τ_{ei} is the electron-ion thermal equilibration time constant [37,38] and is temperature dependent

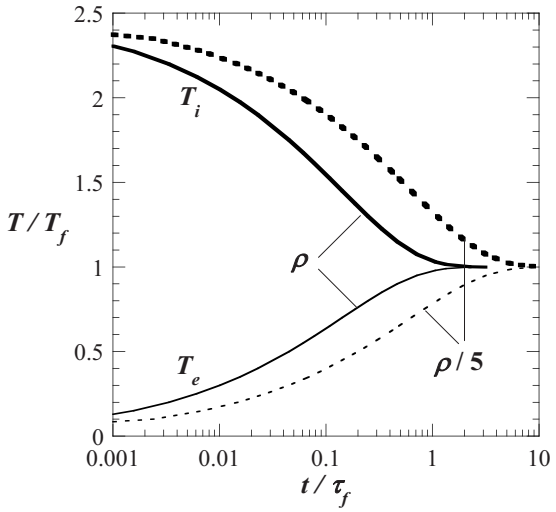

FIG. 6. Electron-ion thermal equilibration for $Z = 1.5$. Ion (bold lines) and electron (thin lines) temperatures approach to within a few percentage of their equilibrium value by time τ_f. Thermal relaxation for plasmas with 1/5 of the reference mass density takes approximately 5 times as long (dotted lines).

$$\frac{\tau_{ei}}{\tau_f} = \left(\frac{T_e}{T_f}\right)^{3/2}, \tag{11}$$

where τ_f is the density-dependent coupling time constant at the equilibrium temperature [4,13,15],

$$\tau_f = \frac{3}{8\sqrt{2\pi}}\left(\frac{4\pi\varepsilon_0}{e^2}\right)^2 \frac{m_i^2}{Z^2 m_e^{1/2}} \frac{T_f^{3/2}}{\rho \ln \Lambda_f}. \tag{12}$$

Here, ρ is the mass density and $\ln \Lambda_f$ is the Coulomb logarithm given by Eq. (7) with $T_e \to T_f$. The small logarithmic dependence of $\ln \Lambda_f$ on temperature has been neglected in Eq. (11).

Using Eqs. (9) and (11), Eq. (10) becomes

$$\frac{dT_e}{dt} = \frac{(1+Z)T_f}{\tau_f} \frac{1 - T_e/T_f}{(T_e/T_f)^{3/2}}. \tag{13}$$

Replacing $T_e/T_f \to \mathrm{T}$ and $t/\tau_f \to t$, the integral representation is

$$(1+Z)\int dt = \int \frac{T^{3/2} dT}{1-T}, \tag{14}$$

which is analytically integrable

$$(1+Z)t = 2\tanh^{-1}[\sqrt{T}] - \frac{2}{3}\sqrt{T}(T+3). \tag{15}$$

Figure 6 is a plot of this relation for $Z = 1.5$.

VI. MEASURING THERMAL EQUILIBRATION

The initial ion temperature T_{0i} imparted by the shock in Eq. (8) depends only on m_i and u_s. The experimental results reported above are consistent with the independence of u_s on the initial gas density ρ_0. Since the same gas composition was used for all experiments, this implies that the converging

shocks launched into capsules with different ρ_0 nonetheless are heated to the same T_{0i}. These situations have coupling rates different by a known factor, since the equilibrium time constant τ depends on ρ_s.

T_{0i} can be estimated using the finite difference form of Eq. (10),

$$\frac{\Delta T_e}{\Delta t} = \frac{T_i - T_e}{\tau_{ei}}. \tag{16}$$

Using Eq. (9) and assuming T_{0e} is negligible, $\Delta T_e = T_e = (T_{0i} - T_i)/Z$ and

$$\frac{T_{0i} - T_i}{\Delta t} = \frac{(1+Z)T_i - T_{0i}}{\tau_{ei}}. \tag{17}$$

If T_i reaches the measured shock-burn-averaged ion temperature T_{si} after Δt equal to half the burn duration Δt_s, then all quantities are known except for T_{i0} and τ_{ei}. These values have a known relationship for high and low ρ_0, so the two sets of measurements are combined to solve for T_{0i}. Using indices 1 and 2 for high and low ρ_0, we obtain

$$\frac{\Delta t_{s2}}{\Delta t_{s1}} \frac{T_{0i} - T_{s1}}{T_{0i} - T_{s2}} = \frac{\tau_{f2}}{\tau_{f1}} \frac{(1+Z)T_{s1} - T_{0i}}{(1+Z)T_{s2} - T_{0i}}. \tag{18}$$

From Table I, $\Delta t_{s2}/\Delta t_{s1} = 0.89$ and from Eq. (12), $\tau_{f2}/\tau_{f1} = 4.5$. Defining $k = (\Delta t_{s2}/\Delta t_{s1})(\tau_{f1}/\tau_{f2})$ and expanding gives a quadratic equation for T_{0i},

$$k(T_{0i} - T_1)[(1+Z)T_2 - T_{0i}] = (T_{0i} - T_2)[(1+Z)T_1 - T_{0i}], \tag{19}$$

with coefficients

$$a = (1-k),$$

$$b = k[(1+Z)T_2 + T_1] - (1+Z)T_1 - T_2,$$

$$c = (1-k)(1+Z)T_1T_2. \tag{20}$$

Using the values from Table I, solutions for T_{0i} at 12.7 and 8.8 keV are obtained. The 12.7 keV solution is rejected as too high compared to observations of T_{si} [39]. The 8.8 keV solution corresponds to an equilibrium temperature $T_f = 3.5$ keV. This is substantially lower than our measured T_{si} of 5.8 (7.7) keV for high (low) ρ_0, indicating that both implosion types are far from thermal equilibrium during the shock burn.

With this shock-burn-averaged estimate of T_{0i}, Eq. (9) and the measurements of T_{si} are used to estimate the shock-burn-averaged electron temperature, giving $T_{se} = 2.0(0.73)$ keV, as stated in Sec. IV. In that section, we also estimated the plasma density ρ_s, which with T_{se} can be used to calculate the shock-burn-averaged τ_{ei} by Eqs. (11) and (12), giving characteristic times of 410 (470) ps [40]. These coupling times are longer than the shock-burn duration, indicating that both implosion types have a large temperature difference at the end of the shock burn.

The initially surprising similarity of the characteristic time constants for high and low ρ_s can be explained by considering that the electrons in the high ρ_s implosion have already absorbed much more thermal energy, thereby increasing the time constant as it takes more collisions to heat them further. More illustrative of the difference in the equilibration rates are the ion temperature relaxation curves according to Eq. (15), plotted in Fig. 7 for high and low ρ_s from an initial temperature $T_{0i} = 8.8$ keV. From the figure, it is evident that the slopes of the two relaxation curves are similar except for very near $t = 0$ when the high ρ_s plasma undergoes rapid equilibration.

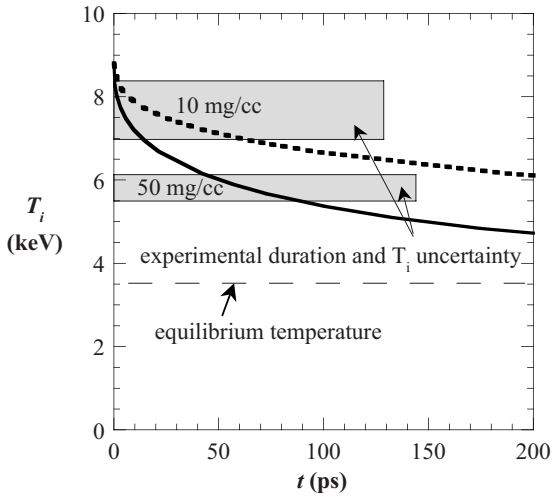

FIG. 7. Ion temperature relaxation for D ^{3}He plasmas of density $\rho_s = 50$ (solid) and 10 (dotted) mg/cm^3. The curves represent the temperature equilibration starting at an initial ion temperature $T_{0i} = 8.8$ keV (corresponding to $T_f = 3.5$ keV). The width of the gray boxes represents the average measured shock-burn duration and the height represents the 1-sigma confidence interval of the experimental shock-burn-averaged ion temperature, T_{si}. Compression-burn overwhelms the shock-burn dynamics starting ~200 ps after shock collapse.

Also shown in Fig. 7 are the measured burn duration and burn-averaged ion temperature T_{si} for implosions with high and low ρ_0. The temperature relaxation curves calculated in the simple model are consistent with the average ion temperature inferred from nuclear yield measurements. However, it should again be noted that the central gas during the shock burn is far from the uniform plasma assumed here, as the shock reflected after collapse will heat the fuel to different initial temperatures at different times as it propagates outwards toward the incoming shell.

VII. CONCLUSIONS

In summary, nuclear production induced by the collapse of strong, spherically convergent shocks was observed using temporal and spectral measurements of products from two distinct, simultaneous nuclear reaction processes. These dual nuclear shock-burn measurements, hitherto unavailable, create a comprehensive description of the state of the implosion immediately after shock collapse time—with gas ion temperatures, gas electron densities, and total areal densities at shock-bang time near 6 keV, 10^{22} e^-/cm^3, and 10 mg/cm^2, respectively.

The extensive information provided by these shock-burn measurements demonstrate that the ions and electrons are far from thermal equilibrium at the end of the shock burn—particularly so for plasmas of lower density. Ion temperature relaxation curves are calculated with a theoretical thermal equilibration model [10] using plasma parameters inferred from shock-yield-averaged measurements. These calculated ion temperature curves—which assume the plasma to be otherwise static and uniform—are consistent with the observed temperatures, despite the dynamic and highly nonuniform plasma state.

Future experiments could explore thermal equilibration in denser plasmas using simple modifications of the methods described herein. For example, the shell could be filled to larger initial density, either with cryogenically cooled gas or alternatively with ^{3}He-wetted, deuterated-plastic foam. Plasmas at much higher areal densities can be investigated with this technique using D ^{3}He protons and DD neutrons if the compression component can be suppressed or significantly delayed, perhaps by using thicker shells, greater energy, or shaped laser pulses. The application of one or more of these modifications would further enhance the *e-i* thermal coupling and push the investigation of temperature equilibration toward the challenging strongly coupled plasma regime.

ACKNOWLEDGMENTS

The authors express their gratitude to the OMEGA engineers and operations crew who supported these experiments. This work was supported in part by the U.S. Department of Energy Office of Inertial Confinement Fusion (Grant No. DE-FG03-03NA00058); the Laboratory for Laser Energetics (Subcontract No. 412160-001G) under Cooperative Agreement No. DE-FC52-92SF19460, University of Rochester; New York State Energy Research and Development Authority; and performed in part under the auspices of the U.S. Department of Energy by Lawrence Livermore National Laboratory under Contract No. DE-AC52-07NA27344.

[1] Ya. B. Zel'dovich and Yu. P. Raizer, *Physics of Shock Waves and High-Temperature Hydrodynamic Phenomena* (Dover Publications, New York, 2002).
[2] J. Nuckolls *et al.*, Nature (London) **239**, 139 (1972).
[3] J. D. Lindl, *Inertial Confinement Fusion* (Springer-Verlag, New York, 1999).
[4] S. Atzeni and J. Meyer-Ter-Vehn, *The Physics of Inertial Fusion* (Oxford University, Oxford, 2004).
[5] D. H. Munro *et al.*, Phys. Plasmas **8**, 2245 (2001).
[6] R. L. McCrory *et al.*, Nucl. Fusion **41**, 1413 (2001).
[7] R. Betti, C. D. Zhou, K. S. Anderson, J. L. Perkins, W. Theobald, and A. A. Solodov, Phys. Rev. Lett. **98**, 155001 (2007).
[8] D. O. Gericke, M. S. Murillo, and M. Schlanges, Phys. Rev. E **65**, 036418 (2002).
[9] L. S. Brown, D. L. Preston, and R. L. Singleton, Jr., Phys. Rep. **410**, 237 (2005).
[10] L. S. Brown and R. L. Singleton, Jr., Phys. Rev. E **76**, 066404 (2007).
[11] M. S. Murillo and M. W. C. Dharma-wardana, Phys. Rev. Lett. **100**, 205005 (2008).
[12] B. Jeon, M. Foster, J. Colgan, G. Csanak, J. D. Kress, L. A. Collins, and N. Gronbech-Jensen, Phys. Rev. E **78**, 036403 (2008).
[13] G. Dimonte and J. Daligault, Phys. Rev. Lett. **101**, 135001 (2008).
[14] L. D. Landau, Phys. Z. Sowjetunion **10**, 154 (1936).
[15] L. Spitzer, *Physics of Fully Ionized Gases* (Wiley, New York, 1962).
[16] P. Celliers, A. Ng, G. Xu, and A. Forsman, Phys. Rev. Lett. **68**, 2305 (1992).
[17] A. Ng, P. Celliers, G. Xu, and A. Forsman, Phys. Rev. E **52**, 4299 (1995).
[18] J. M. Laming *et al.*, Astrophys. J. **472**, 267 (1996).
[19] J. M. Taccetti *et al.*, J. Phys. A **39**, 4347 (2006).
[20] J. J. Angulo Gareta and D. Riley, High Energy Density Phys. **2**, 83 (2006).
[21] R. D. Petrasso *et al.*, Phys. Rev. Lett. **90**, 095002 (2003).
[22] J. A. Frenje *et al.*, Phys. Plasmas **11**, 2798 (2004).
[23] J. R. Rygg *et al.*, Phys. Plasmas **15**, 034505 (2008).
[24] T. R. Boehly *et al.*, Opt. Commun. **133**, 495 (1997).
[25] S. Skupsky *et al.*, Phys. Plasmas **6**, 2157 (1999).
[26] H.-S. Bosch and G. M. Hale, Nucl. Fusion **32**, 611 (1992).
[27] R. A. Lerche *et al.*, Rev. Sci. Instrum. **66**, 933 (1995).
[28] F. H. Séguin *et al.*, Rev. Sci. Instrum. **74**, 975 (2003).
[29] Protons from the shell material are accelerated by electrostatic fields while the laser pulse illuminates the capsule. These fields have decayed well before the time of nuclear production, several 100 ps after the end of the pulse, so do not affect nuclear product spectra. See also D. G. Hicks *et al.*, Phys. Plasmas **8**, 606 (2001).
[30] J. R. Rygg, Ph.D. thesis, Massachusetts Institute of Technology, 2006.
[31] Note that the shock-burn averages discussed in this paper are not direct spatiotemporal averages, but are weighted by the DD-*p* and D^{3}He nuclear production rates, which have strong temperature and density dependence.
[32] C. K. Li *et al.*, Phys. Plasmas **7**, 2578 (2000).
[33] C. K. Li and R. D. Petrasso, Phys. Rev. Lett. **70**, 3059 (1993).
[34] J. H. Gardner *et al.*, J. Fluid Mech. **114**, 41 (1982).
[35] J. R. Rygg, J. A. Frenje, C. K. Li, F. H. Seguin, R. D. Petrasso, V. Y. Glebov, D. D. Meyerhofer, T. C. Sangster, and C. Stoeckl, Phys. Rev. Lett. **98**, 215002 (2007).
[36] R. P. Drake, *High Energy Density Physics* (Springer, New York, 2006).
[37] Note that the parameter τ_{ei}—commonly called the electron-ion equilibration time constant—is not actually constant in time for the large temperature differences considered here.
[38] The large ion-electron mass ratio makes collisions inefficient for exchanging energy between the two species, so generally the individual species will equilibrate on a much faster time scale than the relaxation between the species.

[39] The 12.7 keV root gives T_f=5.1 keV and a characteristic time of 1270 (3660) ps. At peak shock-burn, the corresponding ion temperature would be 8.8 (10.4) keV.

[40] More appropriate to describe the overall shape of the relaxation curve is τ_f, the equilibration time constant at the equilibrium temperature described in Eq. (12): τ_f=880(3900) ps for high (low) ρ_0. However, since $\Delta t_s \ll \tau_f$, τ_f is not suitable for describing the coupling time characteristic of the plasma during shock burn.